

# Instance-Adaptive Keypoint Learning with Local-to-Global Geometric Aggregation for Category-Level Object Pose Estimation

Xiao Zhang, Lu Zou, Tao Lu, Yuan Yao, Zhangjin Huang, *Member, IEEE*, and Guoping Wang

**Abstract**—Category-level object pose estimation aims to predict the 6D pose and size of previously unseen instances from pre-defined categories, requiring strong generalization across diverse object instances. Although many previous methods attempt to mitigate intra-class variations, they often struggle with instances exhibiting complex geometries or significant deviations from canonical shapes. To address this issue, we propose INKL-Pose, a novel category-level object pose estimation framework that enables Instance-adaptive Keypoint Learning with local-to-global geometric aggregation. Specifically, our method first predicts semantically consistent and geometrically informative keypoints using an Instance-Adaptive Keypoint Detector, then refines them: (1) a Local Keypoint Feature Aggregator capturing fine-grained geometries, and (2) a Global Keypoint Feature Aggregator using bidirectional Mamba for structural consistency. To enable bidirectional modeling in Mamba, we introduce a simple yet effective Feature Sequence Flipping strategy that preserves spatial coherence while constructing backward feature sequence. Additionally, we design a surface loss and a separation loss to encourage uniform coverage and spatial diversity in keypoint distribution. The resulting keypoints are mapped to a canonical space for 6D pose and size regression. Extensive experiments on CAMERA25, REAL275, and HouseCat6D show that INKL-Pose achieves state-of-the-art performance with 16.7M parameters and runs at 36 FPS on an NVIDIA RTX 4090D GPU.

**Index Terms**—Object pose estimation, keypoint learning, geometric feature aggregation.

## I. INTRODUCTION

**O**BJECT pose estimation is a fundamental yet challenging problem in computer vision and robotics, with broad applications in robotic grasping [1], autonomous driving [2], and 3D scene understanding [3]. Existing approaches can be broadly classified into instance-level [4]–[9] and category-level [10]–[21] methods. Instance-level methods rely on specific CAD models to estimate the poses of known objects. However, their heavy dependence on accurate CAD models makes them difficult to generalize to real-world scenarios, where objects are often novel and lack corresponding models. This severely limits their applicability to unseen instances within the same category or to objects with variations in shape and appearance. As a more flexible alternative, category-level object pose estimation aims to predict the pose and size of previously unseen instances from predefined object categories. Despite its potential, this task remains considerably

Xiao Zhang, Lu Zou, Tao Lu, and Yuan Yao are with Wuhan Institute of Technology, Wuhan 430205, China (e-mail: xiaozhang@stu.wit.edu.cn, lzou@wit.edu.cn, lut@wit.edu.cn, yaoyuan.usc@gmail.com). Zhangjin Huang is with University of Science and Technology of China, Hefei 230031, China (e-mail: zhuang@ustc.edu.cn). Guoping Wang is with Peking University, Beijing 100871, China (e-mail: wgp@pku.edu.cn). (*Corresponding author: Lu Zou*)

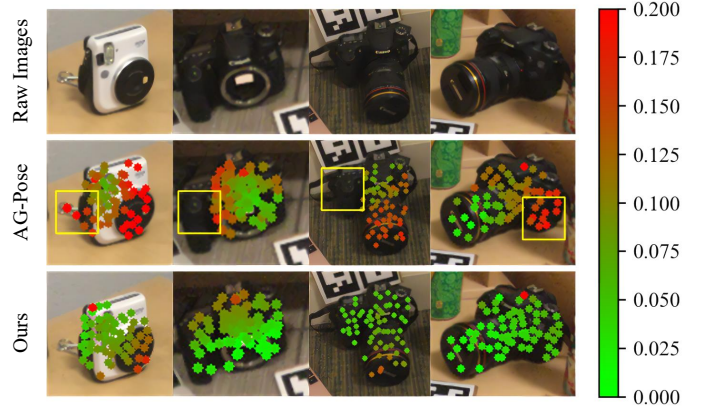


Fig. 1. Visualization of keypoints in NOCS space predicted by AG-Pose [20] and the proposed INKL-Pose on *camera* instances with complex geometry. Keypoint colors indicate their NOCS errors, which are linearly mapped within the range  $[0, 0.2]$  from green (error = 0) to red (error = 0.2). AG-Pose tends to produce clustered and outlier-prone keypoints with higher NOCS errors, whereas INKL-Pose generates spatially diverse and well-distributed keypoints that uniformly cover the object surface with significantly lower errors.

more challenging due to the significant intra-class variations in object shape, texture, and structure.

Recent advances in correspondence-based methods [10]–[14] have shown promising performance in category-level object pose estimation. However, these approaches typically rely on static priors that restrict their adaptability to novel object instances. To address this limitation, shape-prior-free methods [15]–[20] have drawn increasing attention due to their enhanced generalization to novel object instances. Among these methods, AG-Pose [20] proposes a keypoint-based framework that predicts representative keypoints for each instance and establishes keypoint-level correspondences, achieving significant improvements in handling structural discrepancies. Despite its success, AG-Pose derives keypoint features solely from local attention within fixed neighborhoods, combined with a simple global average pooling strategy. This design limits its capacity to capture fine-grained geometric cues and to model global structural consistency. Although AG-Pose incorporates losses to encourage uniformity and separation in keypoint distribution, their effectiveness diminishes when dealing with objects exhibiting complex or irregular geometries. As illustrated in Fig. 1, the resulting keypoints often cluster in limited regions, leading to incomplete surface representation and substantial NOCS errors.

To address the above challenges, we propose INKL-Pose, a novel category-level object pose estimation method that enables instance-adaptive keypoint learning with local-to-global geometric aggregation. Specifically, we first extract and fuse

RGB and point cloud features using a Pointwise Feature Encoder, and then generate a sparse set of semantically consistent and geometrically informative keypoints through an Instance-Adaptive Keypoint Detector. These keypoints are subsequently refined by two complementary modules: (1) a Local Keypoint Feature Aggregator that captures fine-grained geometric details from spatial neighborhoods, and (2) a Global Keypoint Feature Aggregator that utilizes a bidirectional Mamba architecture to model long-range dependencies while maintaining structural consistency across the object. To handle the unordered and non-causal nature of point clouds, we introduce a simple yet effective Feature Sequence Flipping strategy that facilitates bidirectional perception in the feature space while preserving the original spatial structure. Additionally, we design a surface loss and a separation loss to explicitly encourage uniform coverage and spatial diversity among keypoints. The refined keypoints are then mapped to a canonical space to regress the object’s 6D pose and size. As illustrated in Fig. 1, even on complex *camera* instances, the keypoints predicted by our INKL-Pose still achieve accurate and consistent surface coverage, and exhibit significantly lower NOCS errors compared to those predicted by AG-Pose [20].

Overall, our contributions are summarized as follows:

- We propose INKL-Pose, a novel keypoint-based framework for category-level 6D object pose estimation that enables instance-adaptive keypoint learning with local-to-global geometric aggregation.
- We introduce two complementary modules for keypoint feature refinement: a Local Keypoint Feature Aggregator that captures fine-grained geometric details from spatial neighborhoods, and a Global Keypoint Feature Aggregator that leverages bidirectional Mamba with a Feature Sequence Flipping strategy to enable coherent and globally consistent geometric perception.
- We design a surface loss and a separation loss to encourage keypoints to be uniformly and diversely distributed across the object surface, thereby enabling more effective capture of semantically consistent and geometrically informative features.
- Extensive experiments on CAMERA25, REAL275, and HouseCat6D demonstrate that INKL-Pose achieves state-of-the-art performance on both synthetic and real-world benchmarks, significantly outperforming prior methods.

## II. RELATED WORK

In this section, we discuss the literature most relevant to our work from three perspectives: instance-level object pose estimation, category-level object pose estimation, and state space models.

### A. Instance-Level Object Pose Estimation

Instance-level object pose estimation aims to infer the precise pose of an object based on its corresponding 3D CAD model. Existing approaches in this domain can be broadly divided into three categories: direct regression methods [4], [5], direct voting methods [6], [7] and dense 2D-3D correspondence methods [8], [9]. Direct regression methods utilize

end-to-end networks to directly predict the object’s rotation and translation parameters from extracted visual features. Although this approach simplifies the pose estimation pipeline, it suffers from reduced accuracy in cluttered or occluded scenes due to the limitations of direct mapping. Direct voting methods, on the other hand, estimate pose candidates and their corresponding confidence scores at the pixel or point level, ultimately selecting the pose with the highest confidence. While these methods are capable of capturing detailed local information and generally yield strong performance, the dense voting process can be computationally intensive and time-consuming. Alternatively, the third category of instance-level methods follows a correspondence-based paradigm, which first establishes dense 2D–3D correspondences between RGB images and their associated 3D CAD models, and then estimates the object pose using algorithms such as Perspective-n-Point (PnP) or least-squares optimization. Unlike direct regression or voting-based approaches, this method explicitly decouples feature matching from pose estimation, enabling more reliable, geometry-informed inference when accurate correspondences are available. However, their performance heavily relies on the availability of precise CAD models and robust feature descriptors, both of which are often difficult to obtain in real-world scenarios.

### B. Category-Level Object Pose Estimation

Unlike instance-level approaches that rely on known CAD models, category-level 6D object pose estimation aims to estimate the pose and size of previously unseen instances from predefined object categories. This setting is inherently more general and challenging due to substantial intra-class variations among object instances. To address these challenges, NOCS [10] introduces the Normalized Object Coordinate Space, which maps different instances to a unified canonical frame, thereby mitigating variations in scale and geometry. The Umeyama algorithm [22] is then applied to recover the object pose via similarity transformation. To better handle intra-class variations, SPD [11] proposes a deformation network that reconstructs object geometry by learning instance-specific deformations from category-level shape priors, followed by dense correspondence matching between the reconstructed canonical model and the observed point cloud. This paradigm has inspired a series of follow-up works [12]–[14], which further explore the extraction of more robust features and the development of more efficient deformation strategies. However, the static nature of shape priors during both training and inference limits adaptability and hinders generalization to objects with substantial structural variations.

To overcome this limitation, Query6DoF [15] introduces class-specific learnable queries that are jointly optimized with the pose estimation network, enabling the shape priors to adapt dynamically during training. In addition, shape-prior-free methods [16]–[20] have attracted increasing attention for their improved generalization to diverse and unseen object geometries. IST-Net [17] adopts an implicit spatial transformation framework that directly learns correspondences between camera-space and world-space features without relying on explicit priors. CLIPose [16] leverages a vision-language model

to extract rich semantic features from both text and images, aligning them with point cloud representations via contrastive learning. SecondPose [19] integrates geometric features with semantic embeddings from DINOv2 [23], supervised under SE(3)-consistent constraints to improve cross-instance generalization. SpherePose [21] employs a shared spherical proxy representation to address semantic inconsistency arising from shape-dependent canonical spaces. CleanPose [24] integrates causal learning with knowledge distillation to address the spurious correlations introduced by confounding factors in pose estimation. More recently, AG-Pose [20] proposes detecting instance-adaptive keypoints and establishing keypoint-level correspondences to enhance robustness against structural variations across object instances, achieving notable performance improvements.

Our work also focuses on establishing keypoint-level correspondences, but surpasses AG-Pose by introducing a novel keypoint detection method that incorporates explicit constraints on keypoint distribution. Furthermore, our method jointly captures fine-grained geometric details and global structural consistency, enabling the generation of semantically consistent and geometrically informative keypoints. This design provides strong geometric supervision and significantly enhances robustness to intra-class shape variations, ultimately leading to more accurate and generalizable pose estimation.

### C. State Space Models

State Space Models (SSMs) [25], originating from the classical Kalman filter, have attracted increasing interest for their ability to model long-range dependencies with linear computational complexity, while also supporting parallel training. Variants such as S4 [25] introduce diagonal state matrices to reduce memory and computational overhead. Building upon this foundation, Mamba [26] further enhances the SSM framework by incorporating a selective mechanism that compresses context information based on input-dependent parameterization, improving both efficiency and performance. Since the original Mamba operates in a causal manner, where each output token can only attend to preceding tokens, subsequent work such as Vision Mamba [27] introduces bidirectional Mamba to enable information flow in both directions and improve global interaction.

Motivated by these advances, recent studies have adapted the Mamba architecture for 3D point cloud analysis. For instance, PointMamba [28] transforms unordered point cloud data into ordered 1D sequences using Hilbert and Trans-Hilbert curves, preserving spatial continuity and semantic relevance. PCM [29] further utilizes bidirectional Mamba with a point sequence flipping strategy to allow each point to access features from any other point in the cloud. Inspired by the success of Mamba in long-range sequence modeling, we explore its potential for category-level object pose estimation. In particular, we leverage bidirectional Mamba to model globally consistent geometric structures across varied object instances, and propose a novel bidirectional input sequence generation strategy tailored to the unordered and non-causal nature of point cloud data.

## III. METHODOLOGY

### A. Overview

In this section, we present the detailed architecture of the proposed INKL-Pose. As illustrated in Fig. 2, our objective is to jointly estimate an object’s 3D rotation  $R \in \mathbb{R}^{3 \times 3}$ , 3D translation  $t \in \mathbb{R}^3$  and size  $s \in \mathbb{R}^3$  from an input RGB image  $\mathcal{I}_o$  and its corresponding point cloud  $\mathcal{P}_o$ . Specifically, INKL-Pose consists of five key stages. First, the Pointwise Feature Encoder (Section III-B) extracts instance features from both the RGB image and the point cloud, which are subsequently fused to facilitate cross-modal integration. Second, the fused features are processed by the Instance-Adaptive Keypoint Detector (Section III-C) to predict a sparse set of keypoints and their associated features. Third, the Local Keypoint Feature Aggregator (Section III-D) enriches each keypoint with geometrically distinct local features. Fourth, the Global Keypoint Feature Aggregator (Section III-E) captures globally consistent geometric context across object instances. Finally, the Pose and Size Estimator (Section III-F) takes the enhanced keypoints as input and directly regresses the object’s 6D pose and size.

### B. Pointwise Feature Encoder

Given an RGB image  $\mathcal{I}_o$  and its corresponding point cloud  $\mathcal{P}_o$ , the Pointwise Feature Encoder (PFE) extracts informative features from both modalities. Specifically, semantic features  $\mathcal{F}_{\mathcal{I}} \in \mathbb{R}^{N \times d_1}$  are extracted from the RGB image using DINOv2 [23], while geometric features  $\mathcal{F}_{\mathcal{P}} \in \mathbb{R}^{N \times d_2}$  are obtained from the point cloud via PointNet++ [30]. To emphasize relative geometric relationships and reduce the influence of absolute spatial positions, the point cloud is preprocessed by subtracting the mean of all coordinates. Although this operation benefits relative geometry modeling, it reduces the network’s sensitivity to absolute positional cues, which are essential for accurate pose estimation. To compensate for this loss, a Multi-Layer Perceptron (MLP) layer is employed to encode the original spatial coordinates into a latent positional embedding  $\mathcal{E}_{\mathcal{P}} \in \mathbb{R}^{N \times d_3}$ . Finally, the semantic features  $\mathcal{F}_{\mathcal{I}}$ , geometric features  $\mathcal{F}_{\mathcal{P}}$ , and positional embedding  $\mathcal{E}_{\mathcal{P}}$  are concatenated and passed through an additional MLP layer for cross-modal feature fusion, yielding the final pointwise feature representation  $\mathcal{F}_o \in \mathbb{R}^{N \times d}$ , which serves as input for subsequent network modules.

### C. Instance-Adaptive Keypoint Detector

Given the challenges of noise and incomplete observations in cluttered environments, we adopt the Instance-Adaptive Keypoint Detector (IAKD) from AG-Pose [20] as our keypoint generation backbone. This detector formulates keypoint generation as a learnable, query-based process that dynamically generates keypoints from the most informative regions of each object. Specifically, we initialize a learnable keypoint query embedding  $\mathcal{Q}_{kpt}$  set to zero, providing a neutral starting point that avoids bias toward specific patterns. Through multi-head cross-attention and self-attention mechanisms, these query embeddings iteratively interact with the input features  $\mathcal{F}_o$  and



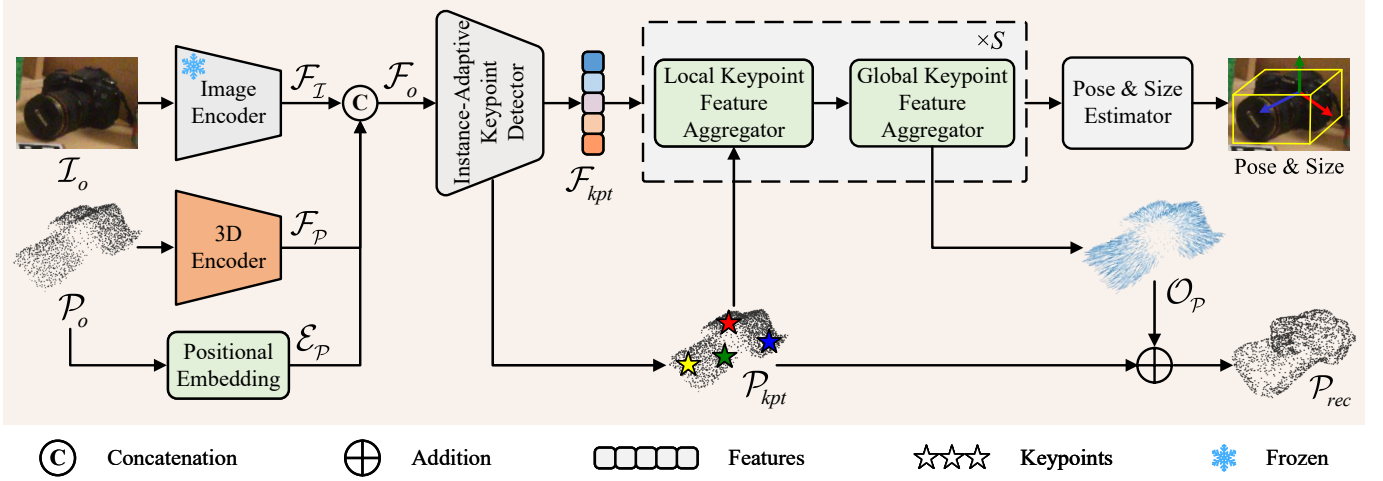


Fig. 2. Overall framework of INKL-Pose. The Instance-Adaptive Keypoint Detector dynamically generates keypoints along with corresponding features using semantic and geometric information extracted by the Pointwise Feature Encoder. The Local Keypoint Feature Aggregator captures fine-grained local structures by aggregating neighborhood information from the point cloud. The Global Keypoint Feature Aggregator models long-range dependencies using bidirectional Mamba, extracting globally consistent geometric representations across instances. The Pose and Size Estimator predicts object rotation, translation, and size from the keypoints and their features.

themselves, progressively refining to capture instance-specific keypoint features. The keypoint probability distribution matrix  $\mathcal{W}$  is computed using cosine similarity followed by a softmax function:

$$\mathcal{W} = \text{Softmax} \left( \frac{\mathcal{Q}_{kpt} \cdot \mathcal{F}_o}{\|\mathcal{Q}_{kpt}\|_2 \cdot \|\mathcal{F}_o\|_2 + \varphi} \right), \quad (1)$$

where  $\varphi$  is a small constant for numerical stability. Based on the matrix  $\mathcal{W}$ , the keypoint coordinates  $\mathcal{P}_{kpt} \in \mathbb{R}^{N_{kpt} \times 3}$  and keypoint features  $\mathcal{F}_{kpt} \in \mathbb{R}^{N_{kpt} \times d}$  are computed as weighted averages of input coordinates  $\mathcal{P}_o$  and fused features  $\mathcal{F}_o$ :

$$\mathcal{P}_{kpt} = \mathcal{W}\mathcal{P}_o, \quad \mathcal{F}_{kpt} = \mathcal{W}\mathcal{F}_o. \quad (2)$$

To ensure the predicted keypoints are both well-distributed across the object surface and geometrically diverse, we introduce two complementary loss functions. First, the surface loss  $\mathcal{L}_{surf}$  encourages uniform surface coverage by minimizing the Chamfer Distance between the predicted keypoints  $\mathcal{P}_{kpt}$  and a set of reference points  $\mathcal{P}_{fps}$ , which are uniformly sampled from the input point cloud using FPS:

$$\mathcal{L}_{surf}(\mathcal{P}_{fps}, \mathcal{P}_{kpt}) = \frac{1}{N_{fps}} \sum_{x_i \in \mathcal{P}_{fps}} \min_{y_i \in \mathcal{P}_{kpt}} \|x_i - y_i\|_2^2 + \frac{1}{N_{kpt}} \sum_{y_i \in \mathcal{P}_{kpt}} \min_{x_i \in \mathcal{P}_{fps}} \|y_i - x_i\|_2^2. \quad (3)$$

Second, the separation loss  $\mathcal{L}_{sep}$  promotes geometric diversity by encouraging each keypoint to be spatially distinct from its local neighbors. Specifically, it maximizes the average pairwise distance between each predicted keypoint and its  $M$ -nearest neighbors in Euclidean space:

$$\mathcal{L}_{sep} = \frac{1}{\max \left( \frac{1}{N_{kpt}} \sum_{i=1}^{N_{kpt}} \frac{1}{M} \sum_{j=1}^M \|\mathcal{P}_{kpt}^i - \text{NN}_j(\mathcal{P}_{kpt}^i)\|_2, \epsilon \right)}, \quad (4)$$

where  $\text{NN}_j(\mathcal{P}_{kpt}^i)$  denotes the  $j$ -th nearest neighbor of the  $i$ -th keypoint, and  $M$  is the number of neighbors considered. In our experiments, we set  $M = 2$ , which provides a lightweight yet effective constraint to mitigate keypoint clustering while maintaining flexibility in spatial layout. The denominator is lower-bounded by a small constant  $\epsilon = 0.01$  to ensure numerical stability.

By jointly optimizing these two loss terms, the predicted keypoints are encouraged to be uniformly distributed and spatially diverse, thus establishing a robust foundation for accurate pose estimation. The effectiveness of these loss functions is demonstrated through ablation studies in Section IV-C.

#### D. Local Keypoint Feature Aggregator

While the extracted keypoints effectively localize salient regions of an object, their sparse nature may result in the loss of fine-grained geometric details. To address this limitation, we propose a Local Keypoint Feature Aggregator (LKFA) that enriches each keypoint by integrating geometrically distinct local features from its surrounding neighborhood.

As illustrated in Fig. 3(a), we first utilize a coordinate encoding function, implemented as an MLP layer, to project the keypoint coordinates into a high-dimensional feature space, producing positional embeddings  $\mathcal{E}_{kpt} \in \mathbb{R}^{N_{kpt} \times d}$ . These embeddings are then added to the initial keypoint features  $\mathcal{F}_{kpt}$  to enhance spatial awareness:

$$\mathcal{E}_{kpt} = \text{MLP}(\mathcal{P}_{kpt}), \quad \mathcal{F}_{kpt} = \mathcal{F}_{kpt} + \mathcal{E}_{kpt}. \quad (5)$$

Next, for each keypoint, we construct a local neighborhood in both coordinate and feature spaces using the  $K$ -nearest neighbor ( $KNN$ ) algorithm. This yields coordinate



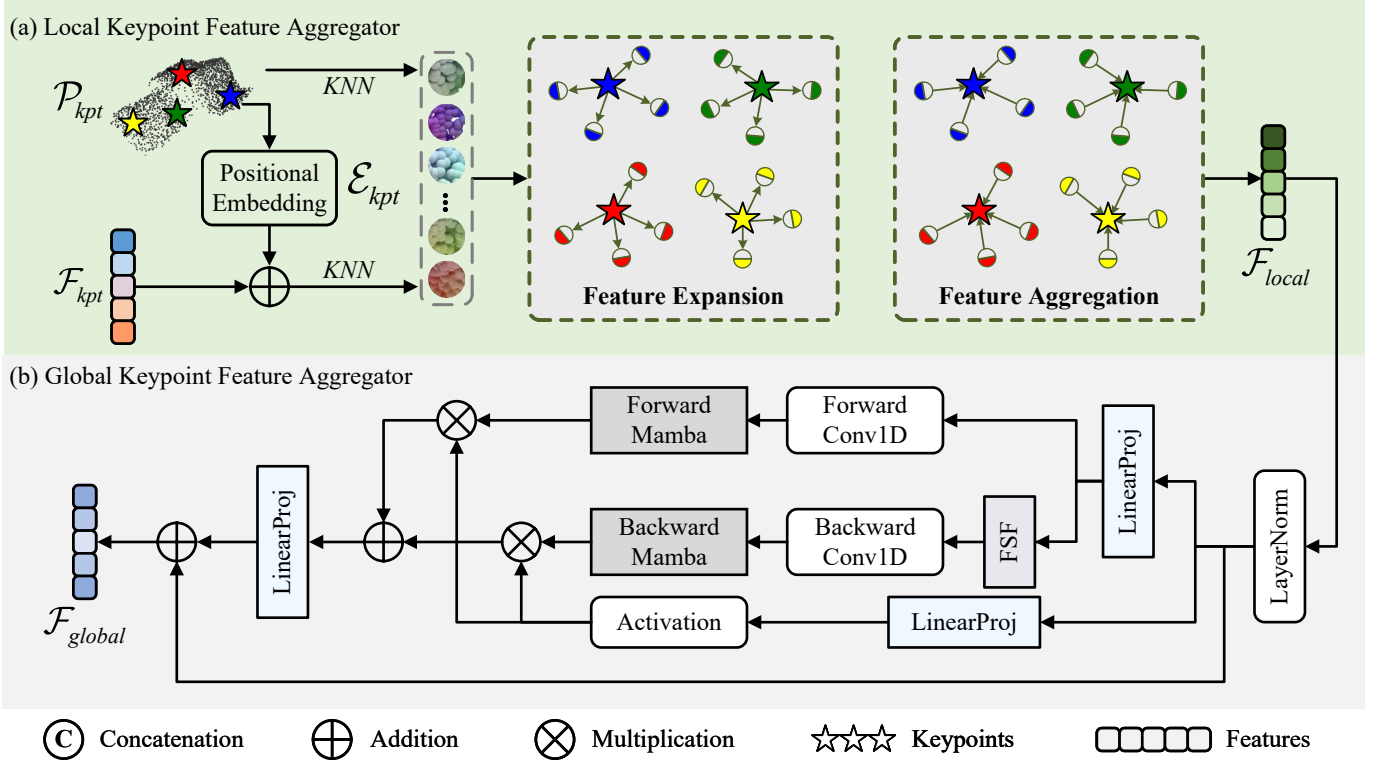


Fig. 3. Illustration of the Local Keypoint Feature Aggregator (LKFA) and Global Keypoint Feature Aggregator (GKFA). (a) LKFA leverages KNN-based neighborhood construction and positional encoding, followed by feature expansion and aggregation, to capture fine-grained geometric details from local neighborhoods. (b) GKFA applies feature sequence flipping to obtain a backward sequence and leverages bidirectional Mamba to model long-range dependencies and global shape structures by integrating both original and flipped feature sequences.

neighborhoods  $\mathcal{P}_K \in \mathbb{R}^{N_{kpt} \times K \times 3}$  and feature neighborhoods  $\mathcal{F}_K \in \mathbb{R}^{N_{kpt} \times K \times d}$ , where  $K$  is the neighborhood size. We then concatenate the spatial and feature descriptors and apply standard normalization to obtain fused local group features  $\mathcal{F}'_K \in \mathbb{R}^{N_{kpt} \times K \times (d+3)}$ , which jointly encode geometric structure and semantic information:

$$\mathcal{F}'_K = \text{Norm}(\text{Concat}(\mathcal{F}_K, \mathcal{P}_K)). \quad (6)$$

To further enhance the representational capacity of each keypoint, we concatenate the normalized neighbor features  $\mathcal{F}'_K$  with the corresponding central keypoint feature  $\mathcal{F}_{kpt}$ , resulting in expanded representations  $\mathcal{F}''_K \in \mathbb{R}^{N_{kpt} \times K \times (2 \times d + 3)}$ . This operation allows each keypoint to incorporate both its own feature and contextual information from its spatial neighborhood. We then apply an affine transformation to  $\mathcal{F}''_K$ , parameterized by learnable weights  $\alpha$  and  $\beta$ , to capture potential rigid transformations in local geometry and adaptively refine the feature distribution. The transformed feature set  $\hat{\mathcal{F}}_K \in \mathbb{R}^{N_{kpt} \times K \times (2 \times d + 3)}$  is computed as follows:

$$\mathcal{F}''_K = \text{Concat}(\mathcal{F}'_K, \mathcal{F}_{kpt}), \quad \hat{\mathcal{F}}_K = \alpha \odot \mathcal{F}''_K + \beta, \quad (7)$$

where  $\odot$  denotes element-wise multiplication.

A max-pooling operation is then applied across each local neighborhood to aggregate the most discriminative geometric and semantic cues into the central keypoint representation.

Finally, an MLP layer is used to refine the output and produce the final local feature representation  $\mathcal{F}_{local} \in \mathbb{R}^{N_{kpt} \times d}$ :

$$\mathcal{F}_{local} = \text{MLP}(\text{MaxPool}(\hat{\mathcal{F}}_K)). \quad (8)$$

By aggregating information from spatially coherent local regions, our LKFA effectively captures geometrically distinct local variations, enhancing the descriptive capacity of each keypoint and laying a solid foundation for robust global perception.

#### E. Global Keypoint Feature Aggregator

While the Local Keypoint Feature Aggregator (LKFA) effectively captures fine-grained geometric details, it lacks the capacity to model global structural context and long-range dependencies among keypoints. To address this limitation, we introduce a Global Keypoint Feature Aggregator (GKFA), which enhances semantic consistency by leveraging SSMs.

As illustrated in Fig. 3(b), GKFA employs a bidirectional Mamba-based architecture [26] to efficiently model long-range dependencies and capture object-level structural information. Compared to traditional Transformers, which suffer from quadratic complexity with respect to sequence length, Mamba operates in linear time, making it a more scalable and efficient choice for processing keypoint sequences in point clouds.

To fully exploit Mamba's bidirectional modeling capabilities, it is necessary to construct both forward and backward feature sequences. A common practice in prior works is

to reverse the input sequence order, a technique we refer to as Point Sequence Flipping (PSF). However, point cloud data lack an inherent spatial order, and reversing the index sequence may place geometrically unrelated keypoints next to each other, thereby disrupting the continuity of feature learning. To address this issue, we propose a simple yet effective strategy termed Feature Sequence Flipping (FSF). Rather than reordering keypoints, FSF reverses the feature channels within each keypoint vector while preserving the original spatial arrangement of the point cloud. Formally, given a keypoint feature vector  $\mathcal{F}_{local}(i) \in \mathbb{R}^d$  expressed as  $[f_1(i), f_2(i), \dots, f_d(i)]$ , we define FSF as:

$$\text{FSF}(\mathcal{F}_{local}(i)) = [f_d(i), f_{d-1}(i), \dots, f_1(i)]. \quad (9)$$

Since different feature channels encode complementary semantics such as geometry or part cues, this reversal introduces a novel perspective on feature dependencies while maintaining the geometric integrity of the point cloud.

In the GKFA, both the original (forward) and FSF-processed (backward) feature sequences are fed into two parallel Mamba blocks. Each block independently captures long-range dependencies within its respective sequence. The outputs from the two Mamba blocks are then aggregated via element-wise summation, forming the final global keypoint features:

$$\mathcal{F}_{global} = \text{SSM}(\mathcal{F}_{local}, \text{FSF}(\mathcal{F}_{local})) + \mathcal{F}_{local}. \quad (10)$$

This design allows the model to incorporate both the original and flipped feature perspectives, promoting more comprehensive global context learning while maintaining computational efficiency and stability.

To ensure that the aggregated keypoints retain meaningful and expressive geometric structure, we utilize the reconstruction-based supervision mechanism [20]. Specifically, we employ an MLP layer to regress dense positional offsets from the global keypoint features. Given  $\mathcal{F}_{global} \in \mathbb{R}^{N_{kpt} \times d}$ , we repeat each feature vector  $m = \lfloor N_{rec}/N_{kpt} \rfloor$  times to construct an expanded representation  $\mathcal{F}'_{global} \in \mathbb{R}^{N_{rec} \times d}$ , where  $N_{rec}$  is the predefined number of reconstruction points (set to 960 in our experiments). The MLP predicts a set of 3D offsets  $\mathcal{O}_{\mathcal{P}} \in \mathbb{R}^{N_{rec} \times 3}$ :

$$\mathcal{O}_{\mathcal{P}} = \text{MLP}(\mathcal{F}'_{global}). \quad (11)$$

Similarly, the keypoint coordinates  $\mathcal{P}_{kpt} \in \mathbb{R}^{N_{kpt} \times 3}$  are repeated  $m$  times to obtain  $\mathcal{P}'_{kpt} \in \mathbb{R}^{N_{rec} \times 3}$ . The reconstructed point cloud  $\mathcal{P}_{rec}$  is then computed as:  $\mathcal{P}_{rec} = \mathcal{P}'_{kpt} + \mathcal{O}_{\mathcal{P}}$ .

To ensure geometric consistency between the reconstructed and observed point clouds, we adopt a Chamfer Distance-based similarity loss  $\mathcal{L}_{sim}$ , which measures the bidirectional alignment between  $\mathcal{P}_{rec}$  and  $\mathcal{P}_o$ :

$$\begin{aligned} \mathcal{L}_{sim}(\mathcal{P}_o, \mathcal{P}_{rec}) = & \frac{1}{N_{pts}} \sum_{x_i \in \mathcal{P}_o} \min_{y_j \in \mathcal{P}_{rec}} \|x_i - y_j\|_2^2 + \\ & \frac{1}{N_{rec}} \sum_{y_j \in \mathcal{P}_{rec}} \min_{x_i \in \mathcal{P}_o} \|y_j - x_i\|_2^2. \end{aligned} \quad (12)$$

To further improve representational capacity, we stack multiple LKFA and GKFA modules, refining keypoint features

hierarchically. Our ablation studies (Section IV-C) show that stacking  $S = 12$  blocks yields the best overall performance.

#### F. Pose and Size Estimator

After obtaining semantically consistent and geometrically informative keypoints and their associated features, we adopt a standard Pose and Size Estimator, as in previous work [14], [20], to infer the object's 6D pose and size. Specifically, we first transform the predicted keypoint coordinates into the NOCS space using the ground-truth rotation  $R_{gt}$ , translation  $t_{gt}$ , and scale  $s_{gt}$ :

$$\mathcal{P}_{kpt}^{gt} = \left\{ \frac{1}{\|s_{gt}\|_2} (x_i - t_{gt}) R_{gt} \mid x_i \in \mathcal{P}_{kpt} \right\}. \quad (13)$$

We then predict the NOCS keypoints from the extracted features via a self-attention mechanism followed by an MLP layer:

$$\mathcal{P}_{kpt}^{nocs} = \text{MLP}(\text{Self-Attn}(\mathcal{F}_{kpt})). \quad (14)$$

To supervise this mapping, we adopt a smooth  $\mathcal{L}_1$  loss:

$$\mathcal{L}_{map} = \frac{1}{N_{kpt}} \sum_{i=1}^{N_{kpt}} \text{Smooth-}L_1 \left( \mathcal{P}_{kpt}^{nocs}(i) - \mathcal{P}_{kpt}^{gt}(i) \right), \quad (15)$$

$$\text{Smooth-}L_1(x) = \begin{cases} 0.5x^2, & \text{if } |x| < 1 \\ |x| - 0.5, & \text{otherwise.} \end{cases} \quad (16)$$

Finally, we regress the object rotation  $R_{pre}$ , translation  $t_{pre}$ , and size  $s_{pre}$  using parallel MLPs based on the concatenated keypoint information:  $\mathcal{F}_{pose} = \text{Concat}(\mathcal{P}_{kpt}, \mathcal{P}_{kpt}^{nocs}, \mathcal{F}_{kpt})$ . We apply an  $\mathcal{L}_2$  loss to supervise these predictions:

$$\mathcal{L}_{pose} = \|R_{pre} - R_{gt}\|_2 + \|t_{pre} - t_{gt}\|_2 + \|s_{pre} - s_{gt}\|_2. \quad (17)$$

#### G. Overall Loss Function

In summary, the overall loss function is as below:

$$\begin{aligned} \mathcal{L}_{all} = & \omega_{sep} \mathcal{L}_{sep} + \omega_{surf} \mathcal{L}_{surf} + \\ & \omega_{sim} \mathcal{L}_{sim} + \omega_{map} \mathcal{L}_{map} + \omega_{pose} \mathcal{L}_{pose}, \end{aligned} \quad (18)$$

where  $\omega_{sep}$ ,  $\omega_{surf}$ ,  $\omega_{sim}$ ,  $\omega_{map}$ , and  $\omega_{pose}$  are hyperparameters used to balance the contributions of separation loss, surface loss, similarity loss, mapping loss and pose loss.

### IV. EXPERIMENTS

#### A. Experimental Setup

1) *Datasets*: Following previous works [20], [21], we evaluate the effectiveness of the proposed INKL-Pose on three widely used benchmarks: CAMERA25 [10], REAL275 [10], and the more challenging HouseCat6D [31] dataset. CAMERA25 is a large-scale synthetic dataset covering six object categories, containing 300k synthetic RGB-D images with objects rendered on virtual backgrounds, of which 25k images are used for evaluation. REAL275 serves as a real-world counterpart to CAMERA25, covering the same six categories. The training set comprises 4.3k images captured from 7 scenes, while the test set includes 2.75k images from 6 different scenes, with three distinct object instances per category.

HouseCat6D is a more complex, real-world multimodal dataset featuring 10 object categories. The training set contains 20k RGB-D images collected across 34 indoor scenes, and the test set includes 3k images from 5 additional scenes. Notably, this dataset poses greater challenges due to its marker-free capture process, dense clutter, and severe occlusion.

2) *Evaluation Metrics*: Following previous works [16], [20], [21], we evaluate the performance of INKL-Pose using two widely adopted metrics.

- $\text{IoU}_x$ . This metric calculates the 3D Intersection-over-Union (IoU) between the predicted and ground-truth bounding boxes. A prediction is considered correct if the IoU exceeds a specified threshold. Following standard protocol, we report  $\text{IoU}_{50}$  and  $\text{IoU}_{75}$  on CAMERA25 and REAL275, and  $\text{IoU}_{25}$  and  $\text{IoU}_{50}$  on the more challenging HouseCat6D dataset.
- $n^\circ\text{mcm}$ . This metric evaluates the 6D pose accuracy by jointly considering rotation and translation errors. A prediction is regarded as correct if the rotation error is less than  $n^\circ$  and the translation error is below  $m$  cm. Following standard protocol, we report results under four commonly used thresholds:  $5^\circ 2\text{cm}$ ,  $5^\circ 5\text{cm}$ ,  $10^\circ 2\text{cm}$ , and  $10^\circ 5\text{cm}$  across all three datasets.

3) *Implementation Details*: We utilize the off-the-shelf Mask R-CNN [32] to generate instance masks and resize all input images to  $224 \times 224$  pixels. For each corresponding object instance, we uniformly sample 1,024 points from the segmented point cloud. To enhance robustness, we apply data augmentation strategies consistent with prior works [14], [20], including random rotations (within 0–20 degrees), translations (in the range of  $-0.02$  to  $0.02$  meters), and scalings (from 0.8 to 1.2). For network configuration, the feature dimensions are set as follows:  $d_1 = 128$ ,  $d_2 = 128$ ,  $d_3 = 64$ , and the fused feature dimension is  $d = 256$ . In the local feature aggregation stage, the neighborhood size  $K$  is set to 4. Additionally, the entire feature aggregation module consists of  $S = 12$  stacked stages, each comprising both local and global aggregation components to progressively refine the keypoint features. In the keypoint generation stage, the network predicts 96 keypoints per object instance. For keypoint supervision, we sample  $N_{fps} = 120$  reference points to ensure sufficient surface coverage and spatial alignment with the predicted keypoints. In the separation loss, the number of nearest neighbors is set to  $M = 2$ , which provides a lightweight yet effective constraint that mitigates keypoint clustering while preserving flexibility in spatial distribution. In the dense point cloud reconstruction stage, each keypoint is repeated 10 times, yielding  $N_{rec} = 960$  reconstructed points. This setting closely matches the resolution of the input point cloud (1,024 points), providing a stable foundation for reconstruction supervision without incurring excessive computational cost.

Regarding optimization, the weights of the loss terms are set as  $\{w_{sep}, w_{surf}, w_{sim}, w_{map}, w_{pose}\} = \{10.0, 10.0, 15.0, 2.0, 0.3\}$ . The model is trained using the Adam optimizer [33] with a cyclical learning rate schedule [34], where the learning rate varies between  $2 \times 10^{-5}$  and  $5 \times 10^{-4}$ . All experiments are conducted on a single NVIDIA RTX 4090D GPU with a batch size of 64. For

CAMERA25 and REAL275, we train the model using both synthetic and real-world data with a synthetic-to-real ratio of 3:1. For HouseCat6D, the model is trained exclusively on its corresponding dataset.

## B. Comparison with State-of-the-Art Methods

1) *Results on REAL275*: Table I reports the performance of INKL-Pose compared with state-of-the-art methods on the REAL275 dataset [10]. As shown in the table, our method exhibits excellent performance on most metrics. Specifically, INKL-Pose achieves 84.0% on  $\text{IoU}_{50}$ , 80.6% on  $\text{IoU}_{75}$ , 63.2% on  $5^\circ 2\text{cm}$ , 68.3% on  $5^\circ 5\text{cm}$ , 80.9% on  $10^\circ 2\text{cm}$ , and 88.0% on  $10^\circ 5\text{cm}$ , demonstrating its strong capability in both pose and size estimation under real-world conditions. Notably, INKL-Pose operates directly on RGB-D input and does not rely on any pre-defined shape priors. Compared with CatFormer [12], the state-of-the-art prior-based method, INKL-Pose achieves significant improvements 15.5% and 14.6%, under the strict  $5^\circ 2\text{cm}$  and  $5^\circ 5\text{cm}$  metrics, respectively. Furthermore, compared to SpherePose [21], the current best-performing shape-prior-free method, INKL-Pose yields performance gains of 5.0% and 0.9% under the strict  $5^\circ 2\text{cm}$  and  $5^\circ 5\text{cm}$  metrics, respectively. In addition, compared to our strong baseline AG-Pose [20], INKL-Pose achieves notable improvements of 6.2% and 3.7% on  $5^\circ 2\text{cm}$  and  $5^\circ 5\text{cm}$  metrics, respectively, highlighting the effectiveness of our fine-to-global geometric aggregation strategy. Qualitative comparisons in Fig. 4 further validate the superiority of INKL-Pose.

2) *Results on CAMERA25*: Table II reports the performance of INKL-Pose compared with state-of-the-art methods on the CAMERA25 dataset. As shown in the table, INKL-Pose achieves outstanding accuracy across nearly all evaluation metrics. Although its  $\text{IoU}_{50}$  metric reaches 94.4%, slightly lower than SpherePose [21] (achieving 94.8%), it significantly outperforms all existing approaches on the remaining metrics, especially under the more rigorous pose accuracy thresholds. Specifically, compared to prior-based methods, INKL-Pose maintains a clear advantage without relying on pre-defined shape priors. In addition, when compared with AG-Pose [20], the current state-of-the-art shape-prior-free method, INKL-Pose achieves notable gains of 1.5% and 1.3% under the strict  $5^\circ 2\text{cm}$  and  $5^\circ 5\text{cm}$  metrics, respectively. These results, along with the strong performance observed on the REAL275 dataset, provide compelling evidence of the robustness and effectiveness of our proposed local-to-global geometric feature aggregation framework. Furthermore, INKL-Pose exhibits strong model efficiency with 16.7M parameters, ranking among the most lightweight methods evaluated except for AG-Pose [20] and GPV-Pose [35]. It also achieves a fast inference speed of 36 FPS on an NVIDIA RTX 4090D GPU, highlighting its potential for real-time applications.

3) *Results on HouseCat6D*: To further validate the generalization capability of the proposed INKL-Pose, we conduct experiments on the more challenging real-world dataset HouseCat6D [31]. As reported in Table III, INKL-Pose achieves state-of-the-art performance across all evaluation metrics. Compared with the current state-of-the-art GCE-Pose [37], our



Method	Prior	REAL275 ( $\uparrow$ )						#Params (M) $\downarrow$
		IoU <sub>50</sub>	IoU <sub>75</sub>	5°2cm	5°5cm	10°2cm	10°5cm	
SPD [ECCV'20] [11]	✓	77.3	53.2	19.3	21.4	43.2	54.1	18.3
SGPA [ICCV'21] [13]	✓	80.1	61.9	35.9	39.6	61.3	70.7	23.3
GPV-Pose [CVPR'22] [35]	✗	83.0	64.4	32.0	42.9	55.0	73.3	<b>8.6</b>
DPDN [ECCV'22] [14]	✓	83.4	76.0	46.0	50.7	70.4	78.4	24.6
IST-Net [ICCV'23] [17]	✗	82.5	76.6	47.5	53.4	72.1	80.5	26.8
Query6DoF [ICCV'23] [15]	✓	82.5	76.1	49.0	58.9	68.7	83.0	19.7
VI-Net [ICCV'23] [18]	✗	-	-	50.0	57.6	70.8	82.1	28.9
CatFormer [AAAI'24] [12]	✓	83.1	73.8	47.7	53.7	69.0	79.5	-
CLIPose [TCSVT'24] [16]	✗	-	-	48.7	58.3	70.4	85.2	-
SecondPose [CVPR'24] [19]	✗	-	-	56.2	63.6	74.7	86.0	38.1
AG-Pose [CVPR'24] [20]	✗	83.8	77.6	56.2	62.3	73.4	81.2	28.9
AG-Pose (DINOv2) <sup>†</sup> [CVPR'24] [20]	✗	84.1	80.1	57.0	64.6	75.1	84.7	11.0
SpherePose [ICLR'25] [21]	✗	84.0	79.0	58.2	67.4	76.2	<b>88.2</b>	-
KeyPose [AAAI'25] [36]	✗	<b>84.2</b>	80.0	57.7	66.0	78.8	88.0	-
GCE-Pose [CVPR'25] [37]	✗	84.1	79.8	57.0	65.1	75.6	86.3	-
<b>Ours<sup>†</sup></b>	✗	<b>84.0</b>	<b>80.6</b>	<b>63.2</b>	<b>68.3</b>	<b>80.9</b>	88.0	16.7

TABLE I

QUANTITATIVE COMPARISONS WITH STATE-OF-THE-ART METHODS ON THE REAL275 DATASET [10]. THE BEST RESULTS ARE IN **BOLD**. THE SYMBOL <sup>†</sup> INDICATES THAT ONLY THE TRAINABLE PARAMETER COUNT IS REPORTED. THE SYMBOL — INDICATES THAT THE DATA IS NOT AVAILABLE OR NOT REPORTED.

Method	Prior	CAMERA25 ( $\uparrow$ )						#Params (M) $\downarrow$
		IoU <sub>50</sub>	IoU <sub>75</sub>	5°2cm	5°5cm	10°2cm	10°5cm	
SPD [ECCV'20] [11]	✓	93.2	83.1	54.3	59.0	73.3	81.5	18.3
SGPA [ICCV'21] [13]	✓	93.2	88.1	70.7	74.5	82.7	88.4	23.3
GPV-Pose [CVPR'22] [35]	✗	92.9	86.6	67.4	76.2	-	87.4	<b>8.6</b>
Query6DoF [ICCV'23] [15]	✓	91.9	88.1	78.0	83.1	83.9	90.0	19.7
VI-Net [ICCV'23] [18]	✗	-	-	74.1	81.4	79.3	87.3	28.9
CatFormer [AAAI'24] [12]	✓	93.5	89.9	74.9	79.8	85.3	90.2	-
CLIPose [TCSVT'24] [16]	✗	-	-	74.8	82.2	82.0	91.2	-
AG-Pose [CVPR'24] [20]	✗	94.1	91.7	77.1	82.0	85.5	91.6	28.9
AG-Pose (DINOv2) <sup>†</sup> [CVPR'24] [20]	✗	94.2	92.5	79.5	83.7	87.1	92.6	11.0
SpherePose [ICLR'25] [21]	✗	<b>94.8</b>	92.4	78.3	84.3	84.8	92.3	-
KeyPose [AAAI'25] [36]	✗	94.4	92.6	79.8	83.6	87.1	92.3	-
<b>Ours<sup>†</sup></b>	✗	94.4	<b>92.9</b>	<b>81.0</b>	<b>85.0</b>	<b>88.1</b>	<b>93.4</b>	16.7

TABLE II

QUANTITATIVE COMPARISONS WITH STATE-OF-THE-ART METHODS ON THE CAMERA25 DATASET [10]. THE BEST RESULTS ARE IN **BOLD**. THE SYMBOL <sup>†</sup> INDICATES THAT ONLY THE TRAINABLE PARAMETER COUNT IS REPORTED. THE SYMBOL — INDICATES THAT THE DATA IS NOT AVAILABLE OR NOT REPORTED.

Method	HouseCat6D ( $\uparrow$ )					
	IoU <sub>25</sub>	IoU <sub>50</sub>	5°2cm	5°5cm	10°2cm	10°5cm
GPV-Pose [35]	74.9	50.7	3.5	4.6	17.8	22.7
VI-Net [18]	80.7	56.4	8.4	10.3	20.5	29.1
SecondPose [19]	83.7	66.1	11.0	13.4	25.3	35.7
AG-Pose [20]	82.4	66.0	11.5	12.6	37.4	42.5
AG-Pose (DINOv2) [20]	88.1	76.9	21.3	22.1	51.3	54.3
SpherePose [21]	88.8	72.2	19.3	25.9	40.9	55.3
GCE-Pose [37]	-	79.2	24.8	25.7	55.4	58.4
<b>Ours</b>	<b>90.8</b>	<b>81.9</b>	<b>25.2</b>	<b>27.4</b>	<b>57.5</b>	<b>61.9</b>

TABLE III

QUANTITATIVE COMPARISONS WITH STATE-OF-THE-ART METHODS ON THE HOUSECAT6D DATASET [31]. THE BEST RESULTS ARE IN **BOLD**.

method surpasses it under all evaluation metric, with gains of 2.7% on IoU<sub>50</sub>, 0.4% on 5°2cm, 1.7% on 5°5cm, 2.1% on 10°2cm, and 3.5% on 10°5cm. Moreover, Fig. 5 presents qualitative results of the predicted poses, further showcasing the strong generalization ability of INKL-Pose in complex real-world scenarios.

4) *Visualization of Predicted Keypoints*: Fig. 6 compares the keypoints predicted by our method with those from the baseline method AG-Pose [20] in the NOCS space. To highlight the differences, keypoints are color-coded based on their NOCS errors, linearly mapped from green (error = 0) to red (error = 0.2). As shown in the figure, AG-Pose produces keypoints with higher NOCS errors and uneven surface coverage. Incorporating our keypoint loss functions into AG-Pose leads to moderate improvements in both accuracy and spatial distribution. In contrast, our INKL-Pose achieves the lowest NOCS errors and generates a more uniform and comprehensive keypoint layout that better captures the object's surface geometry. For example, in the third column showing a mug with a handle, AG-Pose fails to localize the handle, while its variant with our losses partially recovers the region but still exhibits large errors. In comparison, our method accurately delineates the handle contour, resulting in more precise pose estimation.

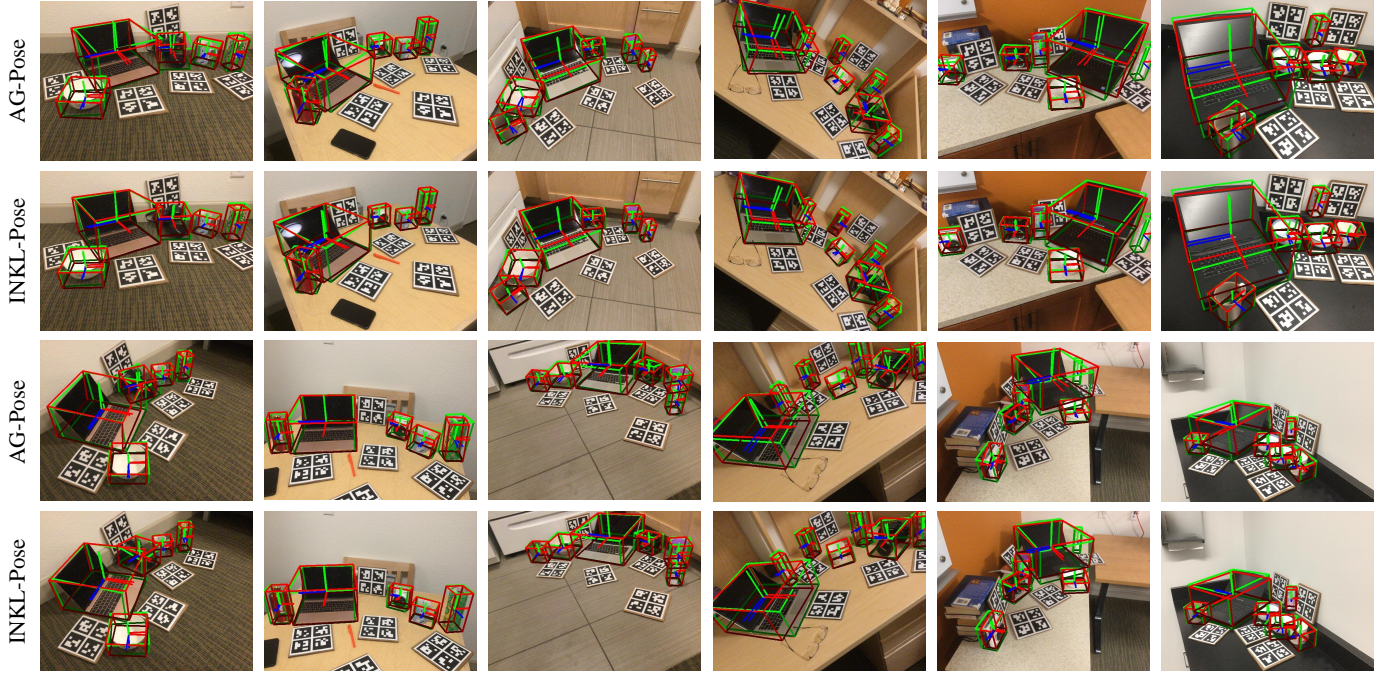


Fig. 4. Qualitative comparisons between INKL-Pose with AG-Pose [20] on the REAL275 dataset, where green and red represent the predicted and ground-truth bounding boxes, respectively. Our INKL-Pose demonstrates superior precision in pose estimation.

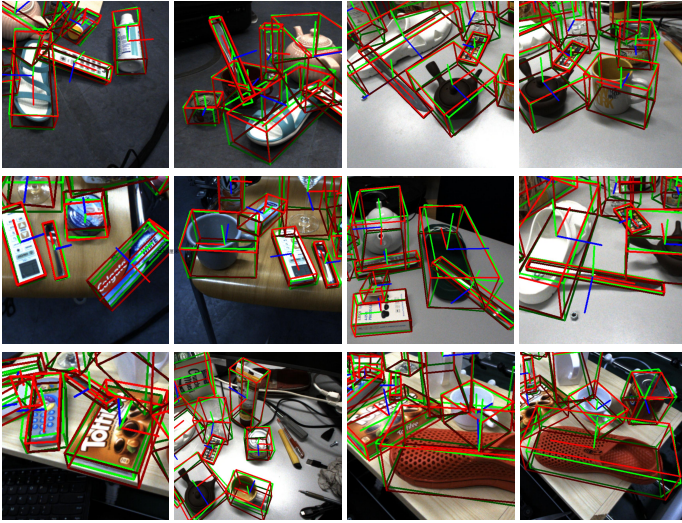


Fig. 5. Visualization results of INKL-Pose on the HouseCat6D dataset. Green bounding boxes denote ground truth, while red bounding boxes represent the predictions from our INKL-Pose. The predicted boxes show high consistency with the ground truth.

### C. Ablation Studies

In this section, we conduct comprehensive ablation studies to evaluate the contributions of key components proposed in INKL-Pose. All experiments are performed on the REAL275 [10] dataset.

1) *Effect of the Number of Keypoints*: We begin by evaluating how the number of predicted keypoints influences the overall pose estimation performance. As shown in Table IV, even with only 16 sparse keypoints, INKL-Pose achieves 56.0% accuracy under the  $5^\circ 2cm$  metric, which is already comparable

$N_{kpt}$	$5^\circ 2cm$	$5^\circ 5cm$	$10^\circ 2cm$	$10^\circ 5cm$
16	56.0	64.3	75.3	85.5
32	57.6	66.0	76.1	87.1
64	59.6	66.7	78.4	87.4
96	<b>63.2</b>	<b>68.3</b>	<b>80.9</b>	<b>88.0</b>
128	59.3	67.7	77.3	87.2

TABLE IV  
EFFECT OF THE NUMBER OF KEYPOINTS. DEFAULT CONFIGURATIONS ARE COLORED IN GRAY, WITH BEST RESULTS HIGHLIGHTED IN BOLD.

Method	$5^\circ 2cm$	$5^\circ 5cm$	$10^\circ 2cm$	$10^\circ 5cm$
w/ ( $\mathcal{L}_{sep} + \mathcal{L}_{surf}$ )	<b>63.2</b>	<b>68.3</b>	<b>80.9</b>	<b>88.0</b>
w/ ( $\mathcal{L}_{div} + \mathcal{L}_{ocd}$ )	60.9	67.0	79.9	87.2
w/ $\mathcal{L}_{sep}$ (Ours)	60.8	67.7	77.8	86.2
w/ $\mathcal{L}_{div}$ (AG-Pose)	59.1	66.9	77.2	86.0
w/ $\mathcal{L}_{surf}$ (Ours)	46.9	53.0	69.1	78.8
w/ $\mathcal{L}_{ocd}$ (AG-Pose)	11.8	18.3	24.7	45.6
None	18.5	20.4	43.7	53.3

TABLE V  
EFFECT OF KEYPOINT SUPERVISION. DEFAULT CONFIGURATIONS ARE COLORED IN GRAY, WITH BEST RESULTS HIGHLIGHTED IN BOLD.

to many existing state-of-the-art methods. As the number of keypoints increases, the performance steadily improves due to a stronger capacity for capturing fine-grained geometric details. The best result is achieved with 96 keypoints, reaching 63.2% on  $5^\circ 2cm$ , which is adopted as the default setting in our framework.

2) *Effect of Keypoint Supervision*: In the Instance-Adaptive Keypoint Detector (IAKD) module (Section III-C), we introduce two auxiliary loss terms,  $\mathcal{L}_{surf}$  and  $\mathcal{L}_{sep}$ , which



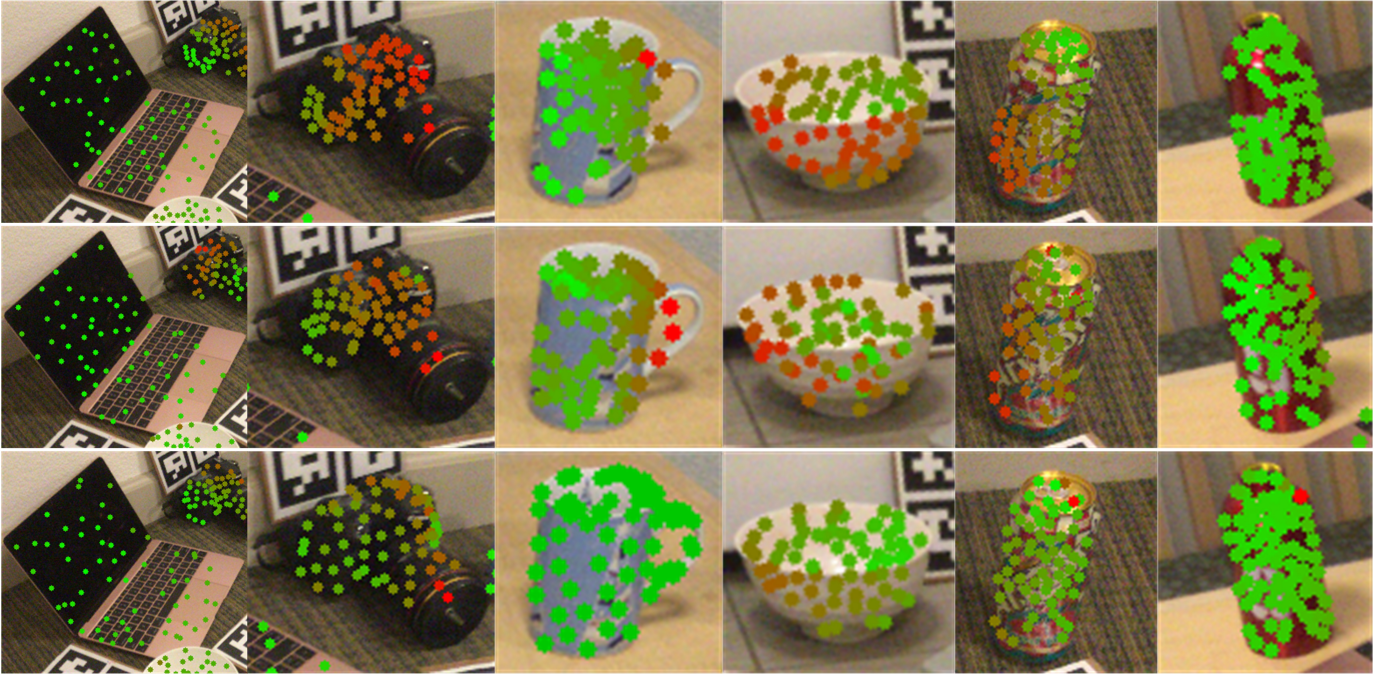


Fig. 6. Comparison of predicted keypoints with the baseline method in NOCS space. The first row shows the results of AG-Pose, the second row shows the results of AG-Pose with the proposed keypoint losses, and the third row shows the results of our INKL-Pose. Keypoint colors indicate their NOCS errors, which are linearly mapped within the range  $[0, 0.2]$  from green (error = 0) to red (error = 0.2).

encourage uniform surface coverage and spatial diversity among keypoints. Table V summarizes the performance under different supervision strategies. As the table shows, without any keypoint supervision (“None”), the model performs poorly across all metrics, highlighting the necessity of proper guidance. When incorporating the surface coverage loss  $\mathcal{L}_{ocd}$  proposed in AG-Pose, the performance further degrades, indicating that this loss is not well suited to our framework. In contrast, the proposed surface loss  $\mathcal{L}_{surf}$  significantly improves performance over the unsupervised baseline.

For keypoint separation, both the  $\mathcal{L}_{div}$  loss from AG-Pose and our proposed  $\mathcal{L}_{sep}$  result in clear performance gains, although  $\mathcal{L}_{sep}$  consistently achieves higher accuracy. Notably, the combination of  $\mathcal{L}_{surf}$  and  $\mathcal{L}_{sep}$  delivers the best performance across all metrics, demonstrating their complementary contributions to keypoint learning. These results confirm that the proposed losses more effectively guide the network to generate semantically consistent, geometrically meaningful, and spatially well-distributed keypoints, which ultimately enhances pose estimation performance.

3) *Effect of Positional Embeddings*: We further analyze the contribution of positional information to feature representation. In INKL-Pose, positional encodings are introduced at two distinct stages: the embedding  $\mathcal{E}_P$  in the Pointwise Feature Encoder (Section III-B), which compensates for the loss of absolute position cues, and  $\mathcal{E}_{kpt}$  in the LKFA module (Section III-D), which enhances local spatial awareness. As reported in Table VI, removing either embedding individually leads to a noticeable performance drop across all metrics, highlighting their complementary roles in capturing geometric information.

Method	5°2cm	5°5cm	10°2cm	10°5cm
Full	<b>63.2</b>	<b>68.3</b>	<b>80.9</b>	<b>88.0</b>
w/o $\mathcal{E}_P$	60.4	67.1	77.6	86.2
w/o $\mathcal{E}_{kpt}$	59.1	66.6	76.9	85.8

TABLE VI  
EFFECT OF POSITIONAL EMBEDDINGS. DEFAULT CONFIGURATIONS ARE COLORED IN GRAY, WITH BEST RESULTS HIGHLIGHTED IN BOLD.

Method	5°2cm	5°5cm	10°2cm	10°5cm
Full	<b>63.2</b>	<b>68.3</b>	<b>80.9</b>	<b>88.0</b>
w/o LKFA	61.1	67.2	80.5	<b>88.4</b>
w/o GKFA	60.2	67.6	77.1	86.6

TABLE VII  
EFFECT OF THE LKFA AND GKFA MODULES. DEFAULT CONFIGURATIONS ARE COLORED IN GRAY, WITH BEST RESULTS HIGHLIGHTED IN BOLD.

4) *Effect of the LKFA and GKFA Modules*: We evaluate the contributions of the LKFA and GKFA modules introduced in Section III-D and Section III-E, respectively. As shown in Table VII, removing the LKFA results in a 2.1% drop in the stringent 5°2cm metric, primarily due to the loss of fine-grained geometric features. Furthermore, removing the GKFA leads to a larger decline of 3.0%, indicating its role in preserving global consistency. These results underscore that both local and global geometric information are crucial for establishing accurate correspondences on unseen objects.

5) *Effect of the Number of LKFA and GKFA Modules*: We investigate the impact of stacking different numbers of keypoint feature aggregation blocks, each containing both a Local Keypoint Feature Aggregator (LKFA) and a Global



$S$	5°2cm	5°5cm	10°2cm	10°5cm
4	59.6	67.5	76.9	86.3
8	61.4	67.0	79.0	86.8
12	<b>63.2</b>	<b>68.3</b>	<b>80.9</b>	<b>88.0</b>
16	60.7	66.9	79.6	87.6

TABLE VIII

EFFECT OF THE NUMBER OF LKFA AND GKFA MODULES. DEFAULT CONFIGURATIONS ARE COLORED IN GRAY, WITH BEST RESULTS HIGHLIGHTED IN **BOLD**.

$K$	5°2cm	5°5cm	10°2cm	10°5cm
1	59.6	67.5	77.6	87.0
2	61.1	68.0	79.2	88.0
4	<b>63.2</b>	<b>68.3</b>	<b>80.9</b>	<b>88.0</b>
6	59.7	68.1	77.9	<b>88.4</b>
8	59.9	67.9	77.0	87.1

TABLE IX

EFFECT OF NEIGHBORHOOD SIZE. DEFAULT CONFIGURATIONS ARE COLORED IN GRAY, WITH BEST RESULTS HIGHLIGHTED IN **BOLD**.

Keypoint Feature Aggregator (GKFA). As shown in Table VIII, increasing the number of blocks from  $S = 4$  to  $S = 12$  consistently improves performance across all metrics, as deeper cascaded aggregation enhances both local and global keypoint representations. However, using  $S = 16$  blocks leads to performance degradation due to feature redundancy and oversmoothing, which reduce keypoint distinctiveness and impair pose estimation. Overall,  $S = 12$  achieves the best balance between accuracy and efficiency.

6) *Effect of Neighborhood Size*: To evaluate the influence of neighborhood size  $K$  in the LKFA module, we vary the number of nearest neighbors used during local feature aggregation. As shown in Table IX, when  $K = 1$ , the model only uses the center point feature, which limits its ability to capture surrounding geometric and semantic context. Increasing  $K$  enhances local structure modeling, with optimal performance achieved at  $K = 4$ . Further increasing  $K$  introduces redundant information, leading to no additional gains.

7) *Effect of Bidirectional Mamba and Feature Sequence Flipping*: We also examine the contributions of the bidirectional Mamba architecture and the proposed Feature Sequence Flipping (FSF) strategy within the GKFA module (Section III-E), as summarized in Table X. The results show that replacing the bidirectional Mamba with its unidirectional counterpart (Uni-Mamba) consistently degrades performance, confirming the advantage of bidirectional modeling for global feature aggregation. Additionally, we compare FSF with the commonly used Point Sequence Flipping (PSF) strategy. PSF exacerbates the non-causal nature of point clouds by reversing the sequence along spatial indices, disrupting the alignment between feature order and geometric structure, and leading to performance drops even below the unidirectional baseline. In contrast, FSF preserves the original point order while achieving bidirectional information flow in feature space, effectively improving robustness to the unordered and non-causal characteristics of point clouds.

Method	5°2cm	5°5cm	10°2cm	10°5cm
Uni-Mamba	60.0	66.6	78.5	86.8
PSF	58.2	65.2	77.0	85.2
FSF	<b>63.2</b>	<b>68.3</b>	<b>80.9</b>	<b>88.0</b>

TABLE X

EFFECT OF BIDIRECTIONAL MAMBA AND FEATURE SEQUENCE FLIPPING. DEFAULT CONFIGURATIONS ARE COLORED IN GRAY, WITH BEST RESULTS HIGHLIGHTED IN **BOLD**.

## V. CONCLUSION

In this paper, we propose INKL-Pose, a novel keypoint-based framework for category-level object pose estimation that enhances generalization to unseen object instances through instance-adaptive keypoint learning and local-to-global geometric aggregation. Specifically, we introduce an Instance-Adaptive Keypoint Detector that predicts semantically consistent and geometrically informative keypoints, along with two complementary modules for feature refinement: a Local Keypoint Feature Aggregator that captures fine-grained geometric details and a Global Keypoint Feature Aggregator based on bidirectional Mamba with a Feature Sequence Flipping strategy for structure-aware global perception. Furthermore, we design a surface loss and a separation loss to explicitly supervise keypoint distribution, providing strong geometric guidance for robust pose estimation. Extensive experiments on CAMERA25, REAL275, and HouseCat6D demonstrate that INKL-Pose achieves state-of-the-art performance across both synthetic and real-world datasets, significantly outperforming existing approaches. In future work, we will focus on extending our framework to dynamic and temporal settings, enabling sequential pose tracking, and explore uncertainty-aware keypoint modeling to further improve robustness under occlusion and sensor noise.

## REFERENCES

- [1] J. Wang, L. Luo, W. Liang, and Z.-X. Yang, "Oa-pose: Occlusion-aware monocular 6-dof object pose estimation under geometry alignment for robot manipulation," *Pattern Recognition*, vol. 154, p. 110576, 2024.
- [2] R. Qian, X. Lai, and X. Li, "3d object detection for autonomous driving: A survey," *Pattern Recognition*, vol. 130, p. 108796, 2022.
- [3] Z. Wu, Z. Wang, S. Liu, H. Luo, J. Lu, and H. Yan, "Fairscene: Learning unbiased object interactions for indoor scene synthesis," *Pattern Recognition*, vol. 156, p. 110737, 2024.
- [4] Y. Di, F. Manhardt, G. Wang, X. Ji, N. Navab, and F. Tombari, "So-pose: Exploiting self-occlusion for direct 6d pose estimation," in *Proceedings of the IEEE/CVF International Conference on Computer Vision*, 2021, pp. 12 396–12 405.
- [5] C. Wang, D. Xu, Y. Zhu, R. Martín-Martín, C. Lu, L. Fei-Fei, and S. Savarese, "Densefusion: 6d object pose estimation by iterative dense fusion," in *Proceedings of the IEEE/CVF conference on computer vision and pattern recognition*, 2019, pp. 3343–3352.
- [6] M. Tian, L. Pan, M. H. Ang, and G. H. Lee, "Robust 6d object pose estimation by learning rgb-d features," in *2020 IEEE International Conference on Robotics and Automation (ICRA)*. IEEE, 2020, pp. 6218–6224.
- [7] G. Zhou, H. Wang, J. Chen, and D. Huang, "Pr-gcn: A deep graph convolutional network with point refinement for 6d pose estimation," in *Proceedings of the IEEE/CVF International Conference on Computer Vision*, 2021, pp. 2793–2802.
- [8] K. Park, T. Patten, and M. Vincze, "Pix2pose: Pixel-wise coordinate regression of objects for 6d pose estimation," in *Proceedings of the IEEE/CVF international conference on computer vision*, 2019, pp. 7668–7677.

- [9] Y. Xu, K.-Y. Lin, G. Zhang, X. Wang, and H. Li, "Rnnpose: 6-dof object pose estimation via recurrent correspondence field estimation and pose optimization," *IEEE Transactions on Pattern Analysis and Machine Intelligence*, vol. 46, no. 7, pp. 4669–4683, 2024.
- [10] H. Wang, S. Sridhar, J. Huang, J. Valentin, S. Song, and L. J. Guibas, "Normalized object coordinate space for category-level 6d object pose and size estimation," in *Proceedings of the IEEE/CVF conference on computer vision and pattern recognition*, 2019, pp. 2642–2651.
- [11] M. Tian, M. H. Ang, and G. H. Lee, "Shape prior deformation for categorical 6d object pose and size estimation," in *Computer Vision—ECCV 2020: 16th European Conference, Glasgow, UK, August 23–28, 2020, Proceedings, Part XXI 16*. Springer, 2020, pp. 530–546.
- [12] S. Yu, D.-H. Zhai, and Y. Xia, "Catformer: Category-level 6d object pose estimation with transformer," in *Proceedings of the AAAI Conference on Artificial Intelligence*, 2024, pp. 6808–6816.
- [13] K. Chen and Q. Dou, "Sgpa: Structure-guided prior adaptation for category-level 6d object pose estimation," in *Proceedings of the IEEE/CVF International Conference on Computer Vision*, 2021, pp. 2773–2782.
- [14] J. Lin, Z. Wei, C. Ding, and K. Jia, "Category-level 6d object pose and size estimation using self-supervised deep prior deformation networks," in *European Conference on Computer Vision*. Springer, 2022, pp. 19–34.
- [15] R. Wang, X. Wang, T. Li, R. Yang, M. Wan, and W. Liu, "Query6dof: Learning sparse queries as implicit shape prior for category-level 6dof pose estimation," in *Proceedings of the IEEE/CVF international conference on computer vision*, 2023, pp. 14 055–14 064.
- [16] X. Lin, M. Zhu, R. Dang, G. Zhou, S. Shu, F. Lin, C. Liu, and Q. Chen, "Clipose: Category-level object pose estimation with pre-trained vision-language knowledge," *IEEE Transactions on Circuits and Systems for Video Technology*, vol. 34, no. 10, pp. 9125–9138, 2024.
- [17] J. Liu, Y. Chen, X. Ye, and X. Qi, "Ist-net: Prior-free category-level pose estimation with implicit space transformation," in *Proceedings of the IEEE/CVF International Conference on Computer Vision*, 2023, pp. 13 978–13 988.
- [18] J. Lin, Z. Wei, Y. Zhang, and K. Jia, "Vi-net: Boosting category-level 6d object pose estimation via learning decoupled rotations on the spherical representations," in *Proceedings of the IEEE/CVF international conference on computer vision*, 2023, pp. 14 001–14 011.
- [19] Y. Chen, Y. Di, G. Zhai, F. Manhardt, C. Zhang, R. Zhang, F. Tombari, N. Navab, and B. Busam, "Secondpose: Se (3)-consistent dual-stream feature fusion for category-level pose estimation," in *Proceedings of the IEEE/CVF Conference on Computer Vision and Pattern Recognition*, 2024, pp. 9959–9969.
- [20] X. Lin, W. Yang, Y. Gao, and T. Zhang, "Instance-adaptive and geometric-aware keypoint learning for category-level 6d object pose estimation," in *Proceedings of the IEEE/CVF Conference on Computer Vision and Pattern Recognition*, 2024, pp. 21 040–21 049.
- [21] H. Ren, W. Yang, X. Liu, S. Zhang, and T. Zhang, "Learning shape-independent transformation via spherical representations for category-level object pose estimation," *arXiv preprint arXiv:2503.13926*, 2025.
- [22] S. Umeyama, "Least-squares estimation of transformation parameters between two point patterns," *IEEE Transactions on Pattern Analysis & Machine Intelligence*, vol. 13, no. 4, pp. 376–380, 1991.
- [23] M. Oquab, T. Darcet, T. Moutakanni, H. Vo, M. Szafraniec, V. Khalidov, P. Fernandez, D. Haziza, F. Massa, A. El-Nouby *et al.*, "Dinov2: Learning robust visual features without supervision," *arXiv preprint arXiv:2304.07193*, 2023.
- [24] X. Lin, Y. Peng, L. Wang, X. Zhong, M. Zhu, J. Yang, C. Liu, and Q. Chen, "Cleanpose: Category-level object pose estimation via causal learning and knowledge distillation," *arXiv preprint arXiv:2502.01312*, 2025.
- [25] A. Gu, K. Goel, and C. Ré, "Efficiently modeling long sequences with structured state spaces," *arXiv preprint arXiv:2111.00396*, 2021.
- [26] A. Gu and T. Dao, "Mamba: Linear-time sequence modeling with selective state spaces," *arXiv preprint arXiv:2312.00752*, 2023.
- [27] L. Zhu, B. Liao, Q. Zhang, X. Wang, W. Liu, and X. Wang, "Vision mamba: Efficient visual representation learning with bidirectional state space model," in *Proceedings of the 41st International Conference on Machine Learning*, 2024, pp. 62 429–62 442.
- [28] D. Liang, X. Zhou, W. Xu, X. Zhu, Z. Zou, X. Ye, X. Tan, and X. Bai, "Pointmamba: A simple state space model for point cloud analysis," *arXiv preprint arXiv:2402.10739*, 2024.
- [29] T. Zhang, H. Yuan, L. Qi, J. Zhang, Q. Zhou, S. Ji, S. Yan, and X. Li, "Point cloud mamba: Point cloud learning via state space model," *arXiv preprint arXiv:2403.00762*, 2024.
- [30] C. R. Qi, L. Yi, H. Su, and L. J. Guibas, "Pointnet++: Deep hierarchical feature learning on point sets in a metric space," *Advances in neural information processing systems*, vol. 30, pp. 5099–5108, 2017.
- [31] H. Jung, S.-C. Wu, P. Ruhkamp, G. Zhai, H. Schieber, G. Rizzoli, P. Wang, H. Zhao, L. Garattoni, S. Meier *et al.*, "Housecat6d-a large-scale multi-modal category level 6d object perception dataset with household objects in realistic scenarios," in *Proceedings of the IEEE/CVF Conference on Computer Vision and Pattern Recognition*, 2024, pp. 22 498–22 508.
- [32] K. He, G. Gkioxari, P. Dollár, and R. Girshick, "Mask r-cnn," in *Proceedings of the IEEE international conference on computer vision*, 2017, pp. 2961–2969.
- [33] D. P. Kingma and J. Ba, "Adam: A method for stochastic optimization," *arXiv preprint arXiv:1412.6980*, 2014.
- [34] L. N. Smith, "Cyclical learning rates for training neural networks," in *2017 IEEE winter conference on applications of computer vision (WACV)*. IEEE, 2017, pp. 464–472.
- [35] Y. Di, R. Zhang, Z. Lou, F. Manhardt, X. Ji, N. Navab, and F. Tombari, "Gpv-pose: Category-level object pose estimation via geometry-guided point-wise voting," in *Proceedings of the IEEE/CVF Conference on Computer Vision and Pattern Recognition*, 2022, pp. 6781–6791.
- [36] S. Yu, D.-H. Zhai, and Y. Xia, "Keypose: Category-level 6d object pose estimation with self-adaptive keypoints," in *Proceedings of the AAAI Conference on Artificial Intelligence*, 2025, pp. 9653–9661.
- [37] W. Li, H. Xu, J. Huang, H. Jung, P. K. Yu, N. Navab, and B. Busam, "Gce-pose: Global context enhancement for category-level object pose estimation," *arXiv preprint arXiv:2502.04293*, 2025.